INTERNATIONAL JOURNAL FOR NUMERICAL METHODS IN FLUIDS, VOL. 7, 29–47 (1987)

# NUMERICAL SIMULATION OF THE HORIZONTAL BRIDGMAN GROWTH. PART I: TWO-DIMENSIONAL FLOW

M. J. CROCHET

*Université Catholique de Louvain, Louvain-la-Neuve, Belgium*

F. T. GEYLING

AND

J. J. VAN SCHAFTINGEN

*Bell Laboratories, Murray Hill, New Jersey, U.S.A.*

SUMMARY

We study the generation of periodic velocity and temperature fields in a plane horizontal crucible of molten metal under the action of a horizontal temperature gradient. The geometry and the boundary conditions are similar to those encountered in the Bridgman growth process of semiconductor crystals, although the present paper is limited to two-dimensional flows. We use transient finite difference and finite element algorithms which lead to identical results. We demonstrate the oscillatory mechanism in two different geometries.

KEY WORDS Finite Elements Transient Flows Three-dimensional Flows Natural Convection Interfaces Oscillatory Flows Crystal Growth Semiconductors Gallium Arsenide

## 1. INTRODUCTION

Several review papers over the last few years have been devoted to the analysis of hydrodynamics of crystal growth; among them, we cite References 1–3. They emphasize the complexity of the phenomena taking place in the melt during the growth of the solid phase. Leaving apart the transfer of impurities, the main problem is to predict the motion of the liquid–solid interface during the complete growth process, and to determine the velocity and temperature distribution in the melt. The problem is not to find an appropriate mathematical model for describing the process; there is no doubt that the Navier–Stokes equations with the Boussinesq approximation coupled with the energy equation are adequate as long as the flow remains laminar (this may not be true for some practical situations where a turbulent regime might be detected). However, the definition of appropriate boundary conditions remains a central preoccupation; the boundary of the flow domain is subject to radiative and convective transfers which are very difficult to specify *a priori* for the existing growth processes.

The main problem lies in the solution of the set of partial differential equations for three main reasons. (i) The geometry of the flow domain changes in time with the motion of the interface. In particular, the boundary of the domain is curvilinear. (ii) The values taken by the non-dimensional

0271–2091/87/010029–19$09.50

*Received 2 April 1986*
*Revised 25 June 1986*

parameters governing the flow in actual processes, i.e. the Grashof and the Rayleigh numbers, make it essentially impossible to use linearized analyses; moreover, at these high values, the flow may bifurcate from a steady-state regime to a periodic flow. (iii) The geometry of actual processes together with experimental results suggest that the flow is truly three-dimensional.

The situation has changed however over the last few years. The development of finite element methods for the solution of the transient Navier–Stokes equations is of considerable help for studying flows in a moving domain with a curvilinear boundary and diverse boundary conditions. The versatility of finite elements for solving such problems is certainly one of their main assets. Simultaneously, the availability of supercomputers allows one to obtain solutions within a reasonable time, although the situation in that respect is still far from ideal. As far as one wishes to obtain a detailed solution which is able to exhibit the short time periodic oscillations in the melt together with the long time motion of the liquid–solid interface, one finds that, even in a two-dimensional flow, the required supercomputer CPU time is of the same order of magnitude as the actual growth process, which is of the order of 24 h.

In the present series of papers, we wish to investigate several aspects of the horizontal Bridgman crystal growth process, and our examples will be based on the growth of gallium arsenide crystals. A typical crucible containing the melt has the shape of a half circular horizontal cylinder with rounded ends. The crucible is surrounded by a furnace which produces a temperature gradient between the ends of the melt. While the crucible is being held fixed, the furnace moves slowly in the horizontal direction, carrying the solid/liquid interface along. The Prandtl number for such flows is of order $10^{-2}$, and typical values for the Grashof number are of the order of $10^6$. Our first two papers in this series will be devoted to the flow in the absence of a growing solid phase, and the third paper will concentrate on the calculation of the interface.

It is well known that periodic temperature oscillations of large amplitude and with periods ranging from a few seconds to a few minutes may occur for many different crystal growth configurations. A qualitative review of the field may be found in Reference 4. Experimental studies on molten gallium performed by Hurle *et al.*[5] show that the oscillations in a rectangular boat, heated and cooled at the opposite ends, set in once critical temperature differential across the boat has been reached. Theoretical explanations of the onset of instability have been suggested by Hart[6] and Gill.[7] They rely upon an idealized two-dimensional steady-state parallel flow upon which one superposes a three-dimensional perturbation. Here, we will limit ourselves to two-dimensional flow analysis. Roughly, we examine the flow in the plane of symmetry of the crucible, with the assumption that the velocity and the temperature gradient vanish in a direction normal to the plane of symmetry. It will be found that a purely two-dimensional mechanism exists for predicting the oscillatory behaviour. In our second paper, however, we will find that the true three-dimensional nature of the geometry has a strong impact upon the flow.

The problem of calculating the plane flow at a high value of the Grashof number has been attacked with different algorithms; a good comparison between their relative results has given us the necessary confidence in our techniques. The occurrence of oscillatory buoyant motion of air in a room was predicted several years ago by Fromm[8] with the development of a transient finite difference code. Our first approach has been to adapt Fromm's explicit method to the calculation of low Prandtl number flows. When the Prandtl number is too small, the maximum time step of the explicit technique is indeed bounded by the calculation of the energy equation. Replacing the explicit temperature calculation by an alternating direction implicit method has allowed us to control the time step by means of the Courant condition.

Simultaneously, we have developed finite element techniques for the eventual calculation of the liquid–solid interface. A classical steady-state technique for solving Navier–Stokes equations[9] has been used together with the transient finite difference code. It was found that the loss of

convergence of the steady-state finite element code would coincide with the emergence of undampened oscillations calculated by means of finite differences. Next, we have extended our finite element code to the calculation of transient flows. Several methods have been tested; a comparison is given by Crochet *et al.*[10] Finally, we have retained the time-stepping technique proposed by Gresho *et al.*[11] which will also be found most suitable in our third paper where we predict the liquid–solid interface.

Having explained the physical problem in section 2, we will review the basic equations in section 3. The finite difference and the finite element methods will be briefly reviewed in sections 4 and 5, respectively. In section 6, we will examine the nature of the steady-state solutions and finally, in section 7, we will analyse the onset of periodic oscillations.

## 2. GEOMETRICAL AND PHYSICAL DATA

A typical boat geometry used for growing gallium arsenide is shown in Figure 1; it has the shape of a half circular cylinder of length $L$ and radius $h$ with rounded ends. An actual value of $L$ is of the order of 20 cm, whereas $h$ is of the order 2·5 cm. During the growth of the gallium arsenide crystal, the domain occupied by the liquid phase reduces in length. The longitudinal temperature gradient imposed on the melt for growing the crystal generates vorticity, and recirculating vortices take place in the crucible. The temperature gradient in actual processes is of the order of 2° C/cm. The cylindrical shape of the boat and the no-slip boundary conditions on the walls would undoubtedly generate a truly three-dimensional motion, which experiments have shown to be time-dependent. Three-dimensional transient calculations are still extremely expensive in computer-time unless one uses a set of coarse numerical approximations. As a first approach, it is instructive to deal with a two-dimensional model problem.

We wish to investigate the flow configuration in the simplified geometry shown in Figure 1. The temperature difference between the end walls is imposed along the x-direction. The $z$-component of the velocity field vanishes and the velocity components and the temperature are $z$-independent. The domain is finite in the $x$ and $y$ directions, and we will consider the flow for various aspect ratios $L/h$. The two-dimensional geometry of the problem is shown in Figure 2.

For the velocity field, we assume that the fluid does not slip along the walls and that the upper

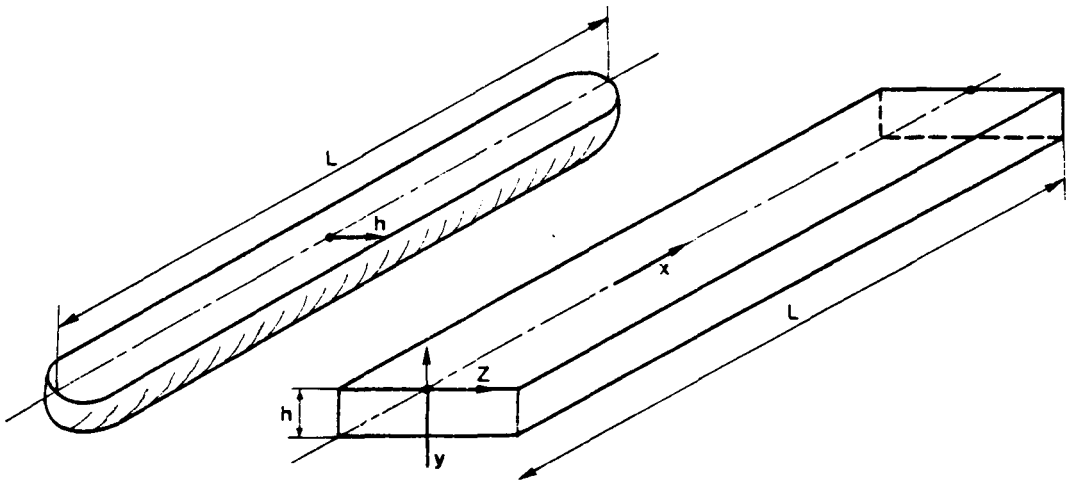


Figure 1. Perspective view of the crucible and idealized geometry

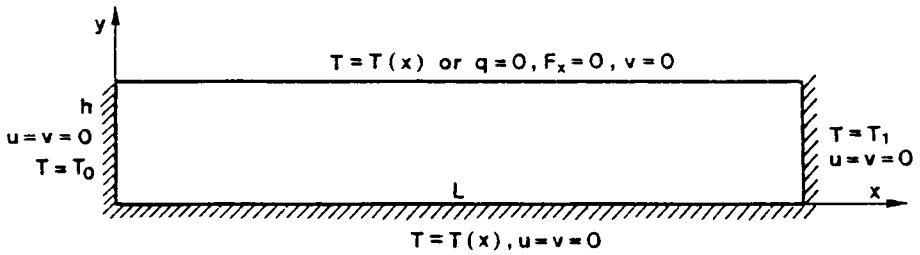


Figure 2. Plane geometry and boundary conditions for the idealized problem

Table I. Physical properties of gallium arsenide

| | | | | | | |
|---|---|---|---|---|---|---|
| Melting point: 1238° C | | | | | | |
| Density $\rho$ in the liquid phase: 5·71 g/cm$^3$ at 1245°C | | | | | | |
| 5·63 g/cm$^3$ at 1320° C | | | | | | |
| Kinematic viscosity: | | | | | | |
| $T$ = 1285 | 1290 | 1295 | 1305 | 1310 | 1325 | °C |
| $\nu$ = 0·320 | 0·297 | 0·280 | 0·266 | 0·260 | 0·254 | cs |

boundary is a free surface of a fixed horizontal shape. Thus, we assume that the tangential force and the normal velocity component vanish on the surface $y = h$. The different boundary conditions applied on the upper and lower surfaces break the symmetry of the problem which would occur in a flow domain surrounded by solid walls.

The thermal boundary conditions are much more difficult to apply. In the actual Bridgman growth, the transparent quartz boat is surrounded by radiating heater elements and an accurate simulation would require the calculation of heat exchanges in a radiating enclosure. In the present paper, we will consider an idealized situation where the temperature is imposed on the walls of the crucible. On the free surface, we will impose two sorts of extreme conditions: (i) the temperature is imposed on the free surface and equals the temperature on the lower wall; (ii) the free surface is thermally insulated. We will find that for the highly conducting fluid being considered here the period of oscillation of the melt is scarcely affected by the thermal boundary condition on the free surface.

The melting point of gallium arsenide is 1238° C and at such a high temperature, accurate data on the physical properties are scarce. Table I shows the values of physical properties given by Glasov *et al.*[12] Data are lacking between the melting point and the lowest temperature of 1285° C in Table I. We will assume that the viscosity $\nu$ keeps a constant value since typical temperature differences in the liquid phase will not exceed 20° C. Whenever an actual value of the viscosity is needed for converting non-dimensional results, we will select the value of 0·5 cs obtained by extrapolation from Table I. From the values of the density at 1245 and 1320° C, one obtains the volumetric coefficient of thermal expansion

$$\alpha = 1{\cdot}9 \times 10^{-4\circ}\,\mathrm{C}^{-1} \tag{1}$$

It is difficult to obtain a precise evaluation of the coefficient of thermal diffusivity $\kappa$ in the liquid phase. For molten metals, it is generally agreed that the Prandtl number $\nu/\kappa$ lies in the range 0·015 to 0·05. Most of the calculations presented here will be based on $Pr = 0{\cdot}015$. A later investigation by Jordan[13] based on a comparison between the solid and the liquid states of gallium arsenide, has led to a value of $Pr = 0{\cdot}069$. Such a value will be adopted for some of the calculations in Part II and III of the present work.

## 3. BASIC EQUATIONS

We wish to solve the two-dimensional form of Navier–Stokes equations with the Boussinesq approximation. Let $T_1$ be a reference temperature (i.e. the melting point) and $\rho_1$ the density at $T_1$. The Navier–Stokes equations are

$$\begin{aligned} -\frac{1}{\rho_1}\frac{\partial p}{\partial x} + \nu\Delta u &= \frac{\partial u}{\partial t} + \frac{\partial u}{\partial x}u + \frac{\partial u}{\partial y}v, \\ -\frac{1}{\rho_1}\frac{\partial p}{\partial y} + \nu\Delta v - \frac{\rho}{\rho_1}g &= \frac{\partial v}{\partial t} + \frac{\partial v}{\partial x}u + \frac{\partial v}{\partial y}v, \\ \frac{\partial u}{\partial x} + \frac{\partial v}{\partial y} &= 0, \end{aligned} \tag{2}$$

where $\Delta$ is the Laplacian operator, $u, v$ are the velocity components in the $x$ and $y$ directions, $p$ is the pressure and $g$ is the gravitational acceleration acting in the negative $y$ direction. The density $\rho$ entering the buoyancy force term depends linearly upon the temperature $T$,

$$\rho = \rho_1[1 - \alpha(T - T_1)]. \tag{3}$$

Equation (3) couples the momentum equations (2) with the energy equation given as follows:

$$\frac{\partial T}{\partial t} + \frac{\partial T}{\partial x}u + \frac{\partial T}{\partial y}v = \kappa\Delta T, \tag{4}$$

where we have assumed that $\kappa$ is temperature-independent and where heat generation by viscous dissipation has been neglected.

It is useful in the present context to introduce non-dimensional variables. We note that the boundary conditions do not provide us with a characteristic velocity associated with the flow; under such circumstances, it is natural to introduce the following non-dimensional, starred quantities:

$$\begin{aligned} x &= hx^*, \qquad y = hy^*, \\ u &= (\nu/h)u^*, \qquad v = (\nu/h)v^*, \\ t &= (h^2/\nu)t^*, \\ T - T_1 &= (T_0 - T_1)T^*, \\ p &= -\rho_1 g y + (\rho_1 \nu^2/h^2)p^*. \end{aligned} \tag{5}$$

The symbol $h$ denotes the depth of the crucible and $(T_0 - T_1)$ is the temperature difference between the end walls. Introducing (5) in (2)–(4) and omitting the stars in the non-dimensional equations, we obtain

$$-\frac{\partial p}{\partial x} + \Delta u = \frac{\partial u}{\partial t} + \frac{\partial u}{\partial x}u + \frac{\partial u}{\partial y}v, \tag{6a}$$

$$-\frac{\partial p}{\partial y} + \Delta v + GrT = \frac{\partial v}{\partial t} + \frac{\partial v}{\partial x}u + \frac{\partial v}{\partial y}v, \tag{6b}$$

$$\frac{\partial u}{\partial x} + \frac{\partial v}{\partial y} = 0, \tag{6c}$$

$$\Delta T = Pr\left(\frac{\partial T}{\partial t} + \frac{\partial T}{\partial x}u + \frac{\partial T}{\partial y}v\right) \tag{6d}$$

For a given aspect ratio and for a given temperature profile between the end walls, the solution depends solely upon the Prandtl number defined in section 2 and the Grashof number $Gr$ defined by

$$Gr = g\alpha(T_1 - T_0)h^3/\nu^2. \tag{7}$$

The term $GrT$ in (6b) gives the importance of the buoyancy force within the flow, whereas $Pr$ indicates the relative importance of heat convection with respect to diffusion. The Rayleigh number of the flow is defined as

$$Ra = Pr\,Gr = g\alpha(T_1 - T_0)h^3/(\kappa\nu). \tag{8}$$

Typical values of the Grashof number for the Bridgman growth of gallium arsenide lie within the range of $5 \times 10^5$ to $5 \times 10^6$.

Finally, with the non-dimensional form (6) of the governing equations, we associate the following set of boundary conditions:

$$\begin{aligned}
&x = 0: && u = v = 0, && T = 1,\\
&x = L/h: && u = v = 0, && T = 0,\\
&y = 0: && u = v = 0, && T = 1 - (xh)/L,\\
&y = 1: && \partial u/\partial y = 0, && v = 0, \qquad T = 1 - (xh)/L \quad \text{or} \quad \partial T/\partial y = 0.
\end{aligned} \tag{9}$$

We will now review the numerical algorithms which have been developed for solving (6) with the boundary conditions (9).

## 4. FINITE DIFFERENCES

Experimental data, together with earlier theoretical results for high values of the Grashof number, indicate that one may expect a time-dependent behaviour of the flow, associated with the occurrence of several vortices and important convective terms in the momentum and the energy equation. In the finite difference literature, Fromm's work[8] shows examples of time-dependent buoyancy driven flows at very high Grashof numbers. Fromm's finite difference algorithm must be slightly modified for calculating flows at a very low Prandtl number.

The finite difference scheme is based on the stream-function–vorticity formulation of the Navier–Stokes equations. Let $\psi$ be the stream function, which is such that

$$u = \frac{\partial \psi}{\partial y}, \quad v = -\frac{\partial \psi}{\partial x}. \tag{10}$$

Equations (6) become, after the elimination of $p$,

$$\begin{aligned}
\frac{\partial T}{\partial t} &= -\frac{\partial (uT)}{\partial x} - \frac{\partial (vT)}{\partial y} + \frac{1}{Pr}\Delta T,\\
\frac{\partial \omega}{\partial t} &= -\frac{\partial (u\omega)}{\partial x} - \frac{\partial (v\omega)}{\partial y} + \Delta\omega + Gr\frac{\partial T}{\partial x},\\
\Delta\psi &= -\omega.
\end{aligned} \tag{11}$$

Fromms' method is entirely explicit as far as the calculation of the time derivatives is concerned. The time integration of (11) is performed in a series of steps which may be briefly schematized as follows. Let $t_n$ be the value of $t$ after the $n$th step, and let $\delta t = t_{n+1} - t_n$. Let $T_n, \psi_n, \omega_n, u_n, v_n$ be the values of the variables associated with time $t_n$; one decomposes the calculation as follows:

$$\begin{aligned}
&\text{(i)} \quad (\tilde{T} - T_n)/\delta t = -\partial(u_n T_n)/\partial x - \partial(v_n T_n)/\partial y,\\
&\text{(ii)} \quad (T_{n+1} - \tilde{T})/\delta t = \Delta\tilde{T}/Pr,\\
&\text{(iii)} \quad (\tilde{\omega} - \omega_n)/\delta t = -\partial(u_n\omega_n)/\partial x - \partial(v_n\omega_n)/\partial y,\\
&\text{(iv)} \quad (\bar{\omega} - \tilde{\omega})/\delta t = \Delta\tilde{\omega},\\
&\text{(v)} \quad (\omega_{n+1} - \bar{\omega})/\delta t = Gr\,\partial T_{n+1}/\partial x,\\
&\text{(vi)} \quad \Delta\psi_{n+1} = -\omega_{n+1}.
\end{aligned} \tag{12}$$

Details on the boundary conditions and the discretization operators may be found in Reference 8; in particular, a fourth-order approximation is used for calculating the convective terms in steps (i) and (iii). The advantage of the explicit algorithm (12) is that (vi) is the only equation requiring the solution of a linear system. Our main problem here has to do with the stability limits for the selection of $\delta t$. Let $\delta x, \delta y$ denote the dimensions of a cell. The successful treatment of convective terms in (i) and (iii) requires compliance with the Courant condition everywhere in the mesh, i.e.

$$\max\left[|u|\delta t/\delta x, \quad |v|\delta t/\delta y\right] \leqslant 1. \tag{13}$$

Simultaneously, the stability of the explicit steps (ii) and (iv) requires that

$$\delta t < \min\left[(\delta x^2, \delta y^2)Pr/4, \quad (\delta x^2, \delta y^2)/4\right]. \tag{14}$$

When the Prandtl number is of order 1, the maximum time step is usually determined by (13), which is valid for implicit as well as explicit schemes. However, when $Pr$ is very low, the first inequality (14) requires very small time steps, and the fully explicit technique is found to be prohibitive. In order to circumvent that difficulty, the explicit step (ii) of (12) is replaced by an implicit one which is unconditionally stable and efficient. We use an alternating direction implicit (Peaceman–Rachford) algorithm[14] which may be summarized as follows. Instead of step (ii), we write

$$\begin{aligned}
\left(1 - \frac{1}{2}\frac{\delta t}{Pr}\frac{\partial^2}{\partial x^2}\right)\bar{T} &= \left(1 + \frac{1}{2}\frac{\delta t}{Pr}\frac{\partial^2}{\partial y^2}\right)\tilde{T},\\
\left(1 - \frac{1}{2}\frac{\delta t}{Pr}\frac{\partial^2}{\partial y^2}\right)T^{n+1} &= \left(1 + \frac{1}{2}\frac{\delta t}{Pr}\frac{\partial^2}{\partial x^2}\right)\bar{T}.
\end{aligned} \tag{15}$$

After discretization, (15) reduces to the solution of two linear tridiagonal systems and, for our low Prandtl number problem, the size of the time step is then governed by (13).

## 5. FINITE ELEMENTS

Let us cover the flow domain with a mesh of quadrilateral finite elements, and let us select the velocity components, the pressure and the temperature as dependent variables. Let $N$ be the number of nodal values associated with $u, v$ and $T$, with shape functions $\psi_i$, and $M$ those associated with $p$, with shape functions $\phi_i$. The finite element representation for the dependent variables is indicated by a star superscript; we write

$$u^* = \sum_{j=1}^{N} U_j \psi_j, \quad v^* = \sum_{j=1}^{N} V_j \psi_j,$$
$$T^* = \sum_{j=1}^{N} T_j \psi_j, \quad p^* = \sum_{j=1}^{M} P_j \phi_j, \tag{16}$$

where $U_j$, $V_j$, $T_j$ and $P_j$ denote nodal values which may depend upon time.

Before performing the space discretization, one needs to obtain the weak form of the set of partial differential equations (6). Let $u'$, $v'$, $T'$, $p'$ denote weighting functions associated with $u$, $v$, $p$ and $T$ respectively. By means of an integration by parts it is easy to obtain the weak equations given as follows:

$$\left\langle \frac{\partial u'}{\partial x}, -p + 2\frac{\partial u}{\partial x} \right\rangle + \left\langle \frac{\partial u'}{\partial y}, \frac{\partial u}{\partial y} + \frac{\partial v}{\partial x} \right\rangle + \left\langle u', \frac{\partial u}{\partial t} + \frac{\partial u}{\partial x}u + \frac{\partial u}{\partial y}v \right\rangle = \langle\langle u', \sigma_x \rangle\rangle,$$
$$\left\langle \frac{\partial v'}{\partial x}, \frac{\partial u}{\partial y} + \frac{\partial v}{\partial x} \right\rangle + \left\langle \frac{\partial v'}{\partial y}, -p + 2\frac{\partial v}{\partial y} \right\rangle + \left\langle v', \frac{\partial v}{\partial t} + \frac{\partial v}{\partial x}u + \frac{\partial v}{\partial y}v \right\rangle - Gr\langle v', T \rangle = \langle\langle v', \sigma_y \rangle\rangle,$$
$$\left\langle p', \frac{\partial u}{\partial x} + \frac{\partial v}{\partial y} \right\rangle = 0 \tag{17}$$
$$\frac{1}{Pr}\left( \left\langle \frac{\partial T'}{\partial x}, \frac{\partial T}{\partial x} \right\rangle + \left\langle \frac{\partial T'}{\partial y}, \frac{\partial T}{\partial y} \right\rangle \right) + \left\langle T', \frac{\partial T}{\partial t} + \frac{\partial T}{\partial x}u + \frac{\partial T}{\partial y}v \right\rangle = \frac{1}{Pr}\langle T', -q \rangle$$

where the simple brackets denote the $L^2$ scalar product over the flow domain and the double brackets indicate the same product along the boundary. The symbol $\sigma_x$, $\sigma_y$ denote the $x$ and $y$ components of the surface force vector, and $q = -\partial T/\partial n$ denotes the outgoing heat flux on the boundary.

In the present paper, we will use the Bubnov–Galerkin formulation. The representations $u^*$, $v^*$, $p^*$, $T^*$ are substituted for $u$, $v$, $p$, $T$ in (17), and the weak form (17) remains valid whenever the weighting functions $u'$, $v'$, $p'$, $T'$ are replaced by one of the shape functions of the associated variable $u$, $v$, $p$ or $T$. Under such circumstances, the weak form (17) indicates that the representations $u^*$, $v^*$ and $T^*$ must be $C^0$-continuous, whereas $p^*$ needs only be $C^{-1}$-continuous. The finite element used in the present investigation is shown in Figure 3; for the velocity components we use a nine-node Lagrangian quadrilateral with biquadratic shape functions. For

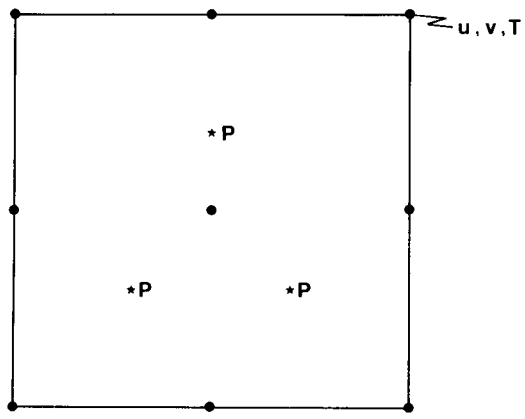


Figure 3. Nine-node quadrilateral element: the velocity components and the temperature are defined at the mid-side nodes and the pressure is a complete first degree polynomial within each element

the pressure, we have found it optimal to use a discontinuous representation. Within each element, the pressure is represented by a complete first-order polynomial. Each additional element within a large mesh introduces eight nodal velocity components and three nodal pressures associated with three incompressibility constraints on the velocity field. A comparison of the performances of several elements for the present application has been given by Crochet *et al.*[10]

Let **V**, **P** and **T** denote the vectors of nodal values for the velocity components, the pressure and the temperature respectively. The application of the Bubnov–Galerkin formulation along the lines which we have just described produces a set of non-linear algebraic equations which may be written in the following symbolic form:

$$\begin{aligned} \mathbf{M}\dot{\mathbf{V}} + \mathbf{K}(\mathbf{V}) + \mathbf{LT} + \mathbf{CP} &= \mathbf{F}, \\ \mathbf{C}^{\mathrm{T}}\mathbf{V} &= \mathbf{0}, \\ \mathbf{M}'\dot{\mathbf{T}} + \mathbf{K}'(\mathbf{V})\mathbf{T} &= \mathbf{F}'. \end{aligned} \tag{18}$$

In (18), **M** and **M**′ are mass matrices, **K**(**V**) and **K**′(**V**) contain the advection-diffusion contributions, **LT** is the discretized buoyancy term, and $\mathbf{C}^{\mathrm{T}}$ is the divergence matrix. The right-hand sides **F** and **F**′ contain the contributions from the boundary conditions.

If the unknown vectors **V**, **T** and **P** in (18) are time-dependent, (18) forms a set of ordinary differential equations with $t$ as the independent variable. In order to describe the time discretization used in the present paper, let us rewrite the system (18) in the compact form

$$\mathbf{A}\dot{\mathbf{Z}} = \mathbf{B}(\mathbf{Z})\mathbf{Z}, \tag{19}$$

where **Z** is the vector of unknowns containing **V**, **P** and **T**. We consider a set of discrete times $t_0, t_1, \ldots, t_n, t_{n+1}, \ldots$; $\mathbf{Z}_n$ is the vector of unknowns at time $t_n$. A comparison of various algorithms has been given by Crochet *et al.*[10] Here, we will briefly review the time-discretization algorithm which we have retained in our later work, and which is a predictor–corrector procedure developed by Gresho *et al.*[11]

In order to show briefly the main steps of the calculation, let us assume that the values of $\mathbf{Z}_{n-1}, \mathbf{Z}_n$ and $\dot{\mathbf{Z}}_{n-1}$ are known.

(i) Using the trapezoidal rule, we calculate the value of $\dot{\mathbf{Z}}_n$ as follows:

$$\tfrac{1}{2}(\dot{\mathbf{Z}}_{n-1} + \dot{\mathbf{Z}}_n) = (\mathbf{Z}_n - \mathbf{Z}_{n-1})/\delta t_{n-1} \tag{20}$$

(ii) We calculate a predicted value $\mathbf{Z}^{\mathrm{p}}_{n+1}$ by means of a second-order extrapolation based on the values $\mathbf{Z}_n$, $\dot{\mathbf{Z}}_{n-1}$ and $\dot{\mathbf{Z}}_n$; one obtains easily

$$\mathbf{Z}^{\mathrm{p}}_{n+1} = \mathbf{Z}_n + \frac{\delta t_n}{2}\left[\left(2 + \frac{\delta t_n}{\delta t_{n-1}}\right)\dot{\mathbf{Z}}_n - \frac{\delta t_n}{\delta t_{n-1}}\dot{\mathbf{Z}}_{n-1}\right] \tag{21}$$

It is not necessary to calculate a predicted value for the pressure **P**.

(iii) Using again the trapezoidal rule, we discretize the system (19) by means of the following second-order approximation in time:

$$\mathbf{A}(\mathbf{Z}_{n+1} - \mathbf{Z}_n)/\delta t_n - \tfrac{1}{2}[\mathbf{B}(\mathbf{Z}_{n+1})\mathbf{Z}_{n+1} + \mathbf{B}(\mathbf{Z}_n)\mathbf{Z}_n] = \mathbf{0}, \tag{22}$$

The non-linear system (22) in $\mathbf{Z}_{n+1}$ is then solved at each time step by means of a Newton–Raphson algorithm. The most efficient procedure is to use $\mathbf{Z}^{\mathrm{p}}_{n+1}$ as the initial guess and to perform only one iteration for solving (22). A sufficient accuracy is maintained provided that the next time step is correctly selected. A procedure for choosing $\delta t_{n+1}$, based on the evaluation of the difference $(\mathbf{Z}_{n+1} - \mathbf{Z}^{\mathrm{p}}_{n+1})$, may be found in Reference 11.

We have seen in section 2 that our problem is characterized by a low value of the Prandtl

number, which reduces the influence of the velocity field upon the evaluation of the temperature field. It has been found quite economical to decouple the problem by first solving the energy equation at each time step and then the equations of motion and the incompressibility constraint. The cost of the calculation is then essentially divided by two.

In later sections, we will also be interested in steady-state results. Rather than calculating the limit of the transient flow, we will then solve the steady-state version of (18), i.e.

$$\begin{aligned} \mathbf{K}(\mathbf{V})\mathbf{V} + \mathbf{LT} + \mathbf{CP} &= \mathbf{F}, \\ \mathbf{C}^{\mathrm{T}}\mathbf{V} &= \mathbf{0}, \\ \mathbf{K}'(\mathbf{V})\mathbf{T} &= \mathbf{F}'. \end{aligned} \tag{23}$$

For solving (23), we use a Newton–Raphson algorithm and iterate until the relative error at a given iteration lies below a pre-assigned bound. A number of four to five iterations is typical for reaching a relative error of $10^{-4}$.

## 6. STEADY-STATE BEHAVIOUR

We have considered three different geometries in our work, with values of the ratio $L/h$ equal to 2, 4 and 8, respectively. The ratio $L/h = 8$ corresponds to a crucible which is, say, 20 cm long and 2·5 cm deep; the ratios 4 and 2 would roughly correspond to the same crucible at various stages of the solidification process. In a subsequent paper, we will calculate the actual shape of the liquid–solid interface. For the finite difference calculations, we have used grids containing $32 \times 16$ cells when $L/h$ is 2 or 4, and $64 \times 16$ cells when $L/h = 8$. For the steady state finite element calculations when $L/h = 4$, we have used a uniform finite element mesh of $16 \times 8$ elements. Since we use nine-node quadrilateral elements, the total number of nodes is the same with our finite difference and steady-state finite element calculations. The transient finite element results have been obtained with a graded finite element mesh of $22 \times 9$ elements when $L/h = 4$; the mesh is shown in Figure 4. All our calculations have been performed with non-dimensional variables, and the solutions are governed by the aspect ratio, the Prandtl number and the Rayleigh or the Grashof number. In our examples, the non-dimensional temperature will be 1 on the left wall and 0 on the right. Isotherms correspond to values of $T = 0, 0{\cdot}1, 0{\cdot}2 \ldots$ In the analysis of the transient behaviour, we have used the non-dimensional time variable defined in (5). The use of a non-dimensional time is not appropriate however for the physical understanding of the results. Whenever we refer to time values or use it as an abscissa, we convert it to a dimensional time based on the values $h = 2{\cdot}5$ cm and $v = 0{\cdot}5$ cs, and thus $t/t^* = 1250$.

With the use of the same dimensional quantities, it is also interesting to translate the values of the Rayleigh and the Grashof numbers into temperature differences between the end walls. Results obtained on the basis of the definition (7) of $Gr$ are given in Table II.

Since each time increment of the flow calculation generates a large file containing the values of the velocity components, the pressure and the temperature, it is convenient to select a scalar

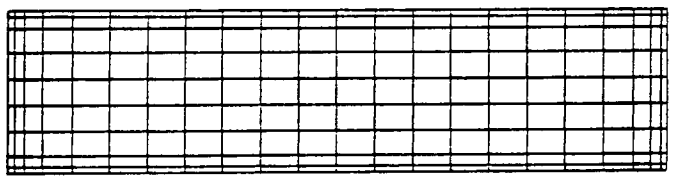

Figure 4. Graded finite element mesh for the aspect ratio $L/h = 4$

Table II. Correspondence between the Rayleigh number, the Grashof number and the actual temperature difference between the end walls when $h = 2{\cdot}5$ cm and $Pr = 0{\cdot}015$

| $Ra$ | $Gr$ | $T_0 - T_1$ |
|---|---|---|
| 1000 | 66,666 | 0·57 |
| 5000 | 333,333 | 2·86 |
| 10,000 | 666,666 | 5·72 |
| 20,000 | 1,333,333 | 11·44 |

parameter for monitoring the transient flow behaviour. We have selected the kinetic energy per unit thickness in the direction perpendicular to the plane of the flow, defined by

$$K = \int_{\Omega} \tfrac{1}{2}\rho(u^2 + v^2)\,\mathrm{d}\Omega, \tag{24}$$

where $\Omega$ is the flow domain. The results will be expressed in terms of a non-dimensional kinetic energy defined as follows:

$$K^* = \int_{\Omega^*} \tfrac{1}{2}(u^{*2} + v^{*2})\,\mathrm{d}\Omega^*, \tag{25}$$

where $\Omega^*$ is the non-dimensional flow domain. The kinetic energy $K^*$ is a global quantity which we have preferred to a local value such as the temperature at one point of the flow domain.

For solving steady-state flows with finite elements, we use the Newton–Raphson algorithm, with the converged solution at a lower value of $Gr$ as a first guess. With the transient finite difference and finite element programs, we suddenly increase the value of $Gr$ (or, equivalently, the temperature difference between the end walls) and use the final state at the lower Grashof number as our initial conditions. Several hundred time steps may be required before a steady-state (or a periodic flow) is reached; typically, the kinetic energy exhibits a significant overshoot which is associated with the flow configuration at the previous value of the Grashof number, until the flow is rearranged and corresponds to the new value of $Gr$.

For our study of the steady-state behaviour, let us concentrate on the aspect ratio $L/h = 4$. When $Gr$ is very low, we expect that the warm particles on the left wall will float towards the cold wall and generate a unicellular flow. At the low value of $Ra = 500$ or $Gr = 33{,}333$ (with an actual temperature difference of 0·28° C between the end walls), one finds that the flow is already characterized by a double cell, and the isotherms are only slightly influenced by the advective terms. Figure 5 shows the growth of $K^*$ as a function of the previously defined dimensional time, and Figure 6 shows the streamlines and the isotherms obtained with finite differences and finite elements, respectively. These solutions have been obtained with a fixed temperature field imposed on the bottom and on the upper surfaces. The finite difference and finite element solutions are the same for all practical purposes and give confidence in the accuracy of the codes. A typical dimensional velocity on the free surface is of the order of 0·3 cm/s.

When $Gr = 66{,}666$, the behaviour of $K^*$ as a function of time, shown in Figure 5, gives a preview of the oscillatory behaviour to be studied in section 7. The present curve corresponds to an insulated free surface; the isotherms, shown in Figure 7, deviate strongly from vertical lines, but the streamlines are little affected by the change of boundary conditions. Indeed, the flow is driven by the horizontal temperature gradient which remains essentially uniform throughout the flow. We find in Figure 5 that a steady-state is not reached after 300 s, and that the period is of the order of

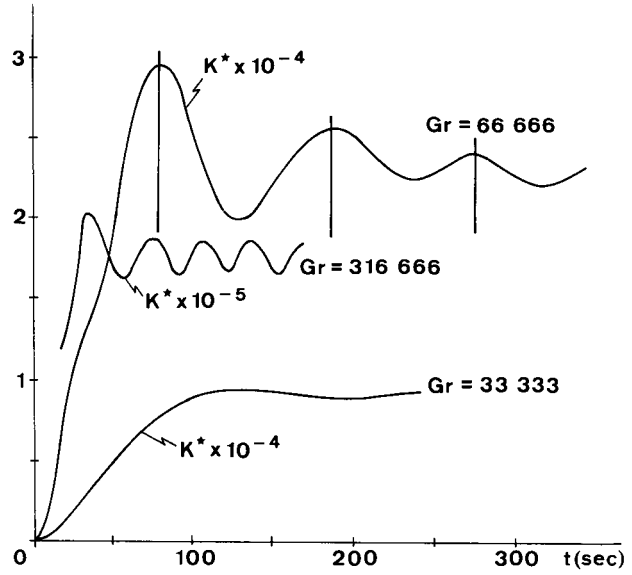


Figure 5. Growth of the non-dimensional kinetic energy as a function of time for $Gr = 33{,}333$, 66,666 and 316,666; $L/h = 4$ and $Pr = 0{\cdot}015$

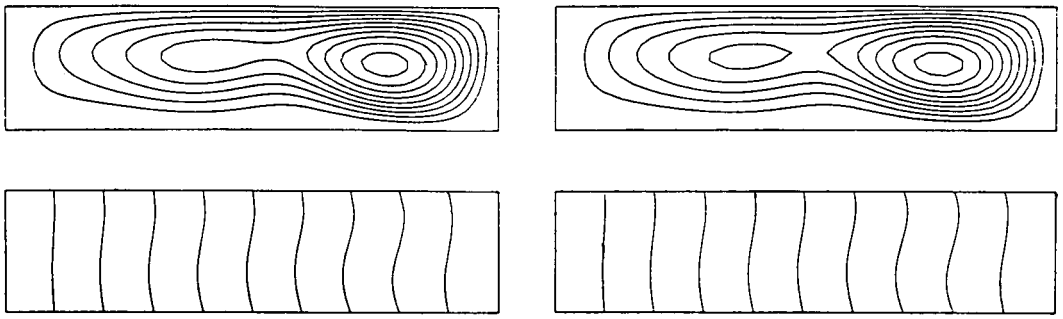

Figure 6. Steady-state streamlines and isotherms at $Gr = 33{,}333$, obtained with finite differences (left) and finite elements (right); the temperature is imposed on the free surface

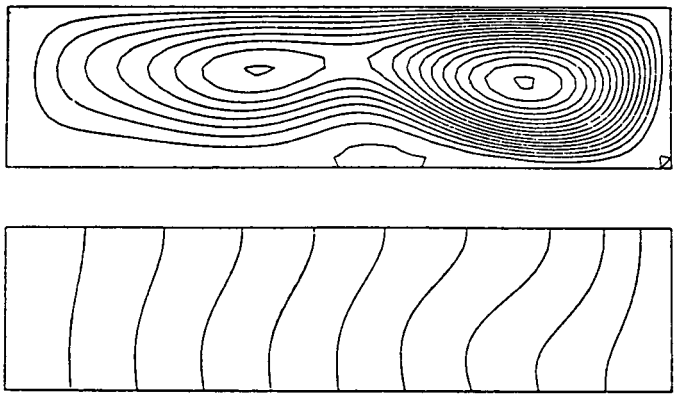

Figure 7. Steady-state streamlines and isotherms at $Gr = 66{,}666$ (finite elements); the heat flux vanishes on the free surface

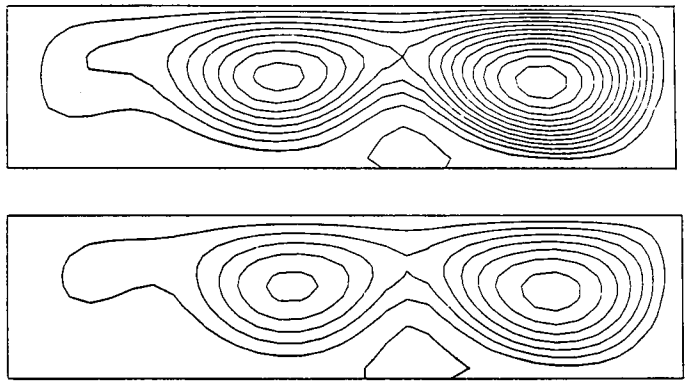

Figure 8. Steady-state streamlines at $Gr = 133{,}333$ and $Gr = 266{,}666$ (finite elements)

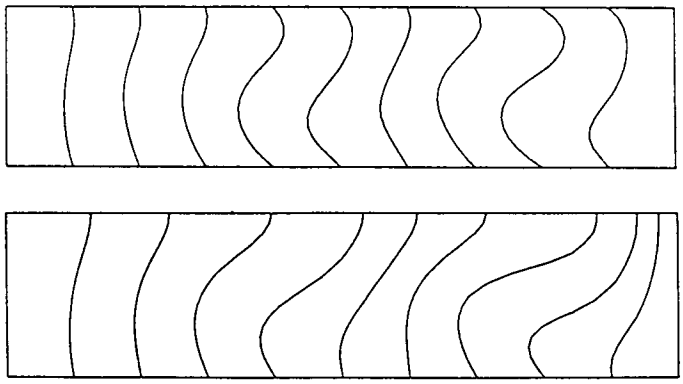

Figure 9. Steady-state isotherms at $Gr = 316{,}666$ (finite elements) with both types of boundary conditions

90 s. A similar behaviour is found for values of $Gr$ equal to 133,333 and 266,666. The steady-state streamlines are shown in Figure 8. The streamlines at $Gr = 266{,}666$ exhibit the flow configuration which will lead to the sustained periodic oscillations at higher values of $Gr$, i.e. three main vortices and two smaller ones in between.

Comparing the behaviour of $K^*$ at $Gr = 33{,}333$ and $Gr = 66{,}666$ as a function of time in Figure 5, we may expect that the oscillatory behaviour will become undampened at some value of $Gr$. Indeed, $Gr = 316{,}666$ is the highest value for which it is possible to obtain a steady-state solution with the finite element program which solves the system (23). Beyond that value, Newton–Raphson iterations cease to converge, even with very small increments in $Gr$. For the same value of $Gr = 316{,}666$, the finite difference program, starting from the solution at a lower value of $Gr$, exhibits a periodic curve for the kinetic energy shown in Figure 5, with a period of 31·6 s based on an average of three periods. The same case has been run with our finite element transient code on a graded mesh. It is again found that the oscillatory behaviour is essentially undampened at $Gr = 316{,}666$ with a period of 33 s as compared with 31·6 s from finite differences. Such minor discrepancies may be expected since our finite difference code is of the first order in time whereas the finite element code is of the second order. The important result is that the steady-state program loses convergence and both transient programs give rise to an undampened oscillation at the same value of $Gr$. The isotherms of the steady solution at $Gr = 316{,}666$ are shown in Figure 9 for the two types of boundary conditions. One finds that the isotherms in the cold region (where

solidification occurs) are now much more affected by advection, in particular when the heat flux vanishes on the free surface. The velocity component on the free surface is of the order of 1·4 cm/s, with a temperature difference of 2·7° C across the boat.

## 7. OSCILLATORY BEHAVIOUR

We have found in section 6 that the steady-state flow configuration is subdivided into several vortices. Their length across the boat is not uniform. We must indeed recall that the upper boundary is a free surface; the material particles accelerate freely on the free surface, and the symmetrical pattern which we might expect within a cavity made of no-slip walls is lost. When the temperature gradient increases, the oscillatory behaviour which is detected in the generation of the vortices gets undampened. We wish now to investigate more closely the kinematics of the periodic motion with $L/h$ equal to 4 and 8, respectively, when the temperature profile is imposed on the upper and on the lower boundaries.

Figure 10 shows curves of the kinetic energy as a function of time obtained with finite elements when $L/h$, whereas Figure 11 shows similar curves obtained with finite differences when $L/h = 8$. Again, a dimensional time has been used for the physical interpretation of the results. Typically, the kinetic energy climbs to a maximum value, with a flow configuration similar to its initial value. The occurrence of the maximum is followed by a rapid decrease of the kinetic energy, which tends rapidly to a periodic behaviour. One should observe that the pattern of the kinetic energy is faithfully reproduced at each period; this is quite noticeable on the second graph of Figure 10. When $Gr$ is high, a true periodic pattern is not reached even after several hundred time steps. In Figure 11, we find that, for $Gr = 2{,}666{,}666$, a small period of 13 s is superposed upon a period of about 50 s.

Table III gives the values of the period found as a function of $Gr$ and $L/h$, and these results are shown on the plot of Figure 12. It is clear that the period of oscillation decreases when $Gr$ increases. In comparing results with $L/h = 4$ and 8, respectively, it is found that $Gr$ defined by (7) may not be the optimal non-dimensional parameter. Considering that the flow is driven by the horizontal temperature gradient, it would be desirable to find the same value of $Gr$ for $L/h = 4$ and 8 when the temperature gradient is the same. Thus, instead of (7), we would use

$$Gr' = g\alpha \frac{T_1 - T_0}{L} h^4/\nu^2 = Gr \frac{h}{L}. \tag{26}$$

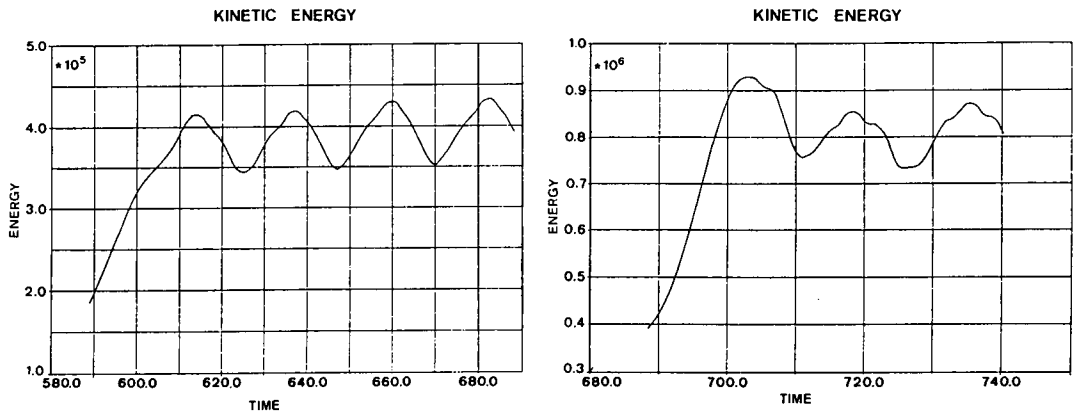


Figure 10. Behaviour of the non-dimensional kinetic energy as a function of time for $Gr = 666{,}666$ and $Gr = 1{,}333{,}333$, obtained with finite elements; the aspect ratio $L/h = 4$

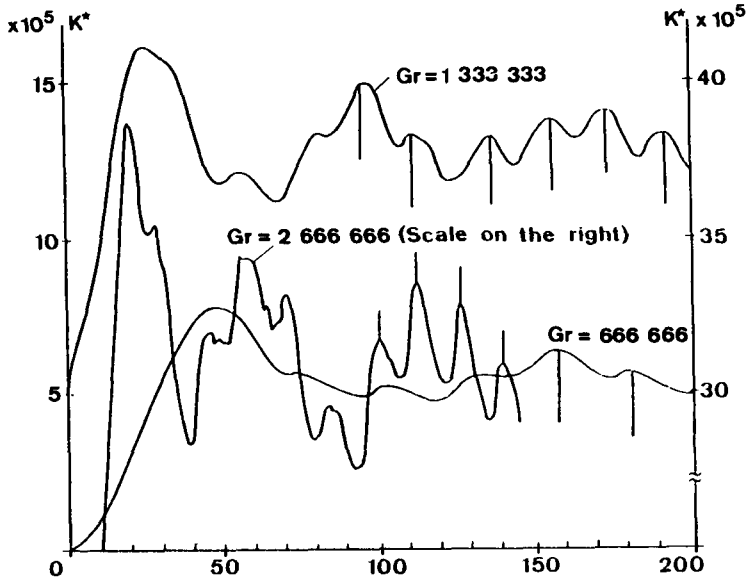


Figure 11. Behaviour of the non-dimensional kinetic energy as a function of time for $Gr$ = 666,666, 1,333,333 and 2,666,666, obtained with differences; the aspect ratio $L/h = 8$

Table III. Period of oscillation as a function of the Grashof number when $L/h = 4$ and 8, respectively, obtained with finite elements and finite differences

| $Gr$ | $L/h$ | $Gr'$ | Period (FD) | Period (FE) |
|---|---|---|---|---|
| 316,666 | 4 | 79,166 | 31·5 | 33 |
| 666,666 | 4 | 166,666 | 20 | 22 |
| 1,333,333 | 4 | 333,333 | 15 | 17 |
| 3,333,333 | 4 | 833,333 | 6·5 | — |
| 666,666 | 8 | 83,333 | 27 | — |
| 1,333,333 | 8 | 166,666 | 19·25 | — |
| 2,666,666 | 8 | 333,333 | 13 | — |

The values of $Gr'$ are given in Table III, and the second plot of Figure 12 shows the period as a function of $Gr'$. We note that, under such circumstances, we obtain very similar values for both aspect ratios. Again, we find that the periods obtained with finite elements are about 10 per cent higher than those obtained with finite differences.

Let us now examine the kinematics of the flow as a function of time throughout a period. Figure 13 shows a typical period when $L/h = 4$ and $Gr$ = 1,333,333, obtained with finite differences (although the finite element results are identical), which is representative of all results found with the same aspect ratio. The flow contains essentially five vortices. The main vortex on the cold wall is fairly stable whereas the other four alternate in size and intensity. At this high value of $Gr$, the isotherms deviate considerably from the vertical, and their shape oscillates with the periodic growth and decay of the vortices. In Figure 14, we show the streamlines and the isotherms when $L/h = 8$ for $Gr$ = 2,666,666. The value of $Gr'$ is the same for Figures 13 and 14, and we find that the patterns of the streamlines are very similar in the neighbourhood of the cold wall.

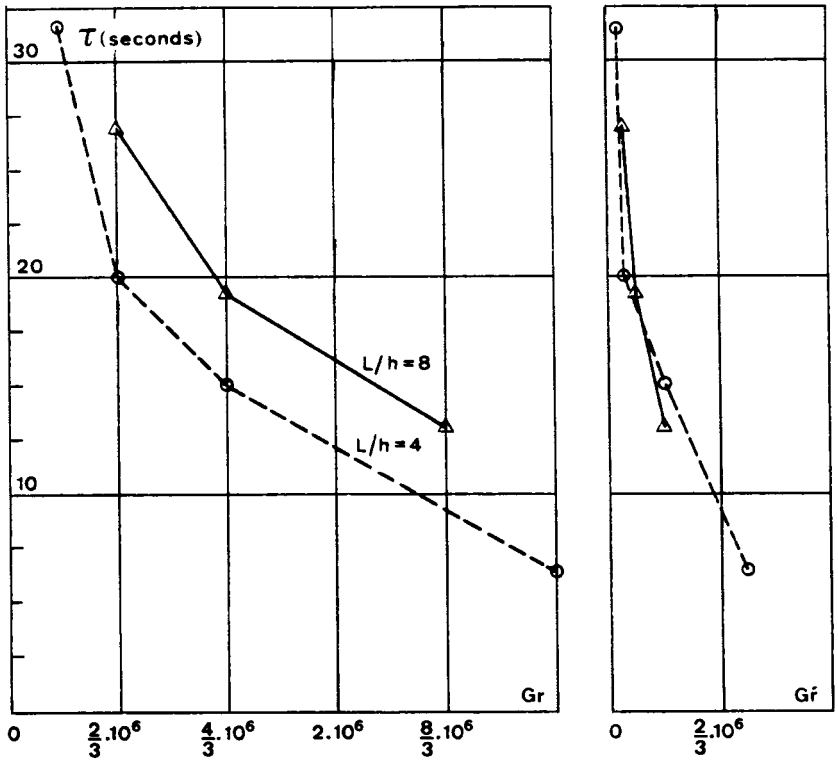


Figure 12. Plot of the period of oscillation in the melt as a function of $Gr$ and $Gr'$, for $L/h = 4$ and 8; finite difference results

We have also calculated the flow for $L/h = 4$ when instead of imposing the temperature field on the free surface, we assume that the heat flux vanishes. For $Gr = 666{,}666$, one finds (with finite differences) a period of 17·5 s, compared with 20 s found when the temperature is imposed on the free surface. The streamlines throughout a period are essentially the same with both types of boundary conditions, whereas the isotherms are strongly affected by the periodic motion, since they are not attached to the upper boundary.

Finally, we have calculated the flow when $L/h = 4$ and the temperature profile is imposed on the free surface, with a Prandtl number of 0·05 instead of 0·015. Since the flow is driven by the horizontal temperature gradient, we may expect similar behaviours when $Pr = 0{\cdot}015$ and $Pr = 0{\cdot}05$, provided that $Gr$ remains identical. However, heat convection should be more important when $Pr = 0{\cdot}05$. A steady state finite element solution has been found up to $Gr = 400{,}000$ with $Pr = 0{\cdot}05$, against $Gr = 316{,}666$ with $Pr = 0{\cdot}015$. At $Gr = 666{,}666$, the flow is oscillating with a period of 19 s against 20 s with $Pr = 0{\cdot}015$. The streamlines show the same pattern in both situations, but the isotherms are much more distorted at the higher value of $Pr$. A typical transient flow pattern is shown in Figure 15.

## 8. CONCLUSIONS

In the present paper, we have described a two-dimensional mechanism for the onset of periodic oscillations in a melt under the action of a horizontal temperature gradient. Steady-state finite element and time-dependent finite difference and finite element methods have been adapted to the

study of low Prandtl number flows. There is total agreement between the results obtained with these different techniques. The loss of convergence of the steady-state finite element method coincides with the onset of oscillations detected by the time-dependent methods. The order of magnitude of the periods of oscillation agrees with experimental data.

The possibility of three-dimensional perturbations has been omitted at the outset. In later papers, we will investigate the effect of finite lateral boundary conditions upon the flow.

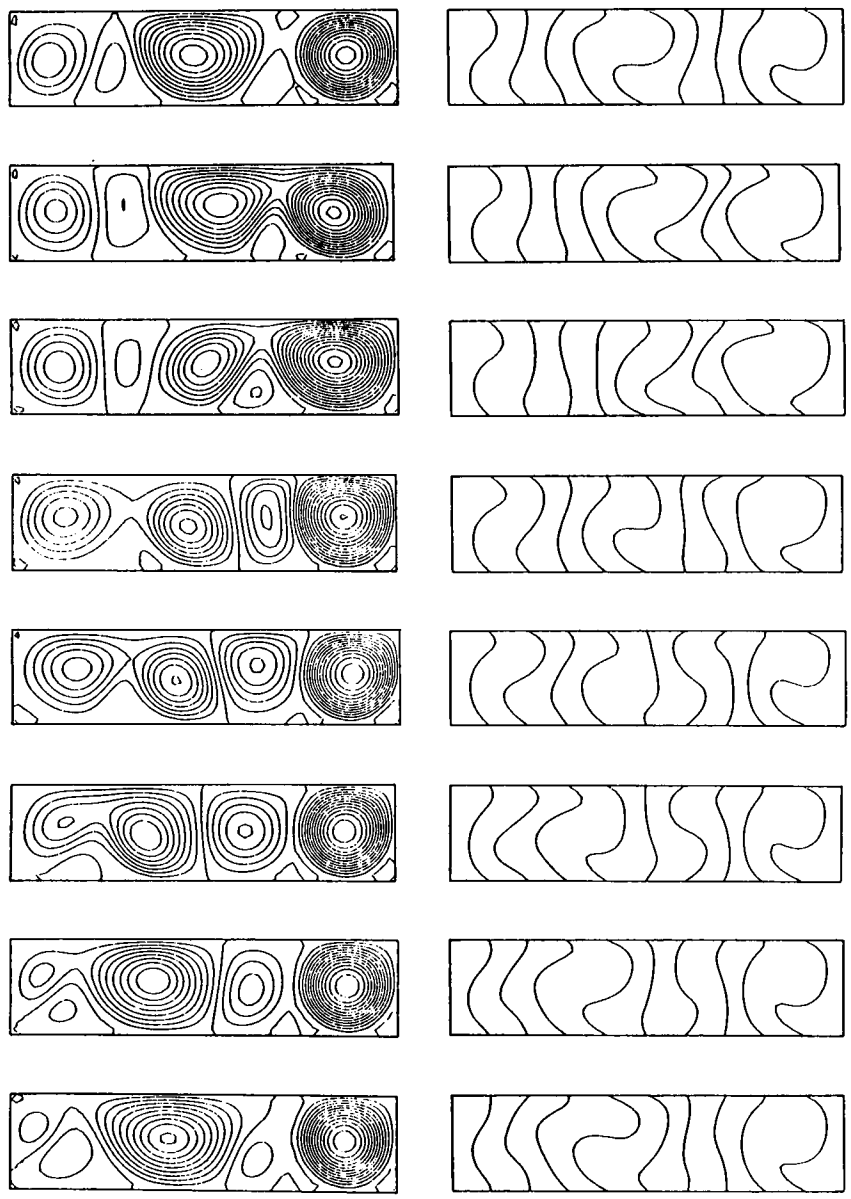

Figure 13. Streamlines and isotherms during a full period of oscillation at $Gr = 1{,}333{,}333$ with $L/h = 4$; finite difference results. A graph is shown every two seconds

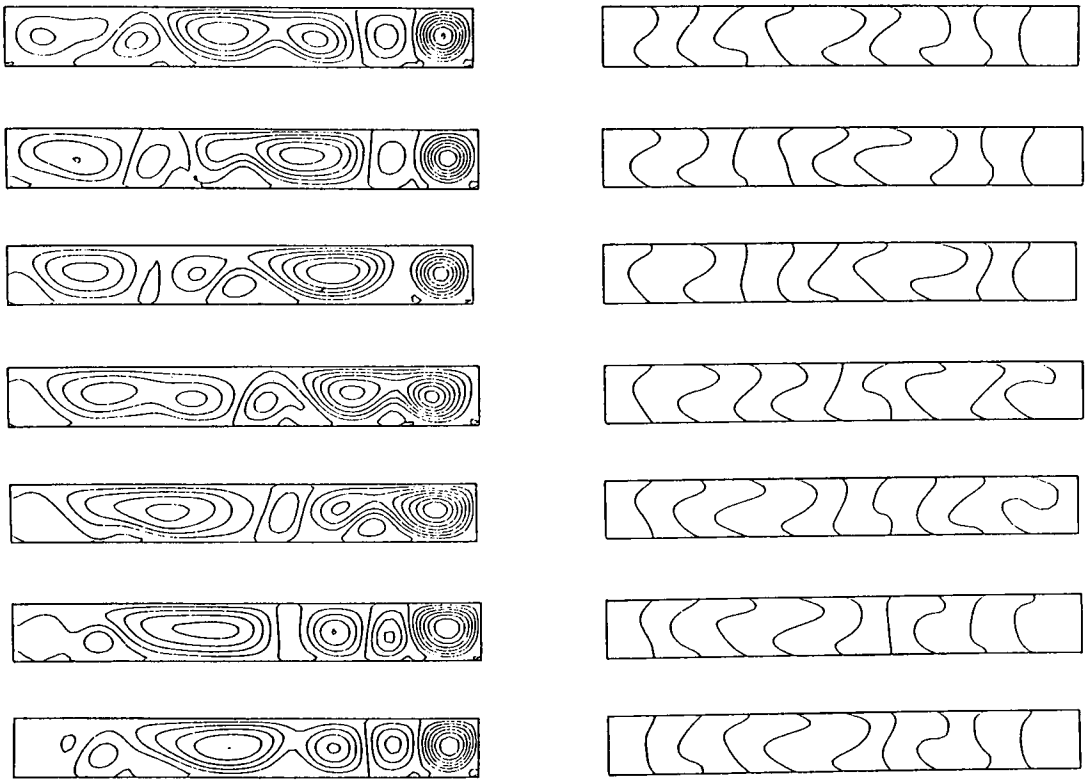

Figure 14. Streamlines and isotherms during a full period of oscillation at $Gr = 2{,}666{,}666$ with $L/h = 8$; finite difference results. A graph is shown every two seconds

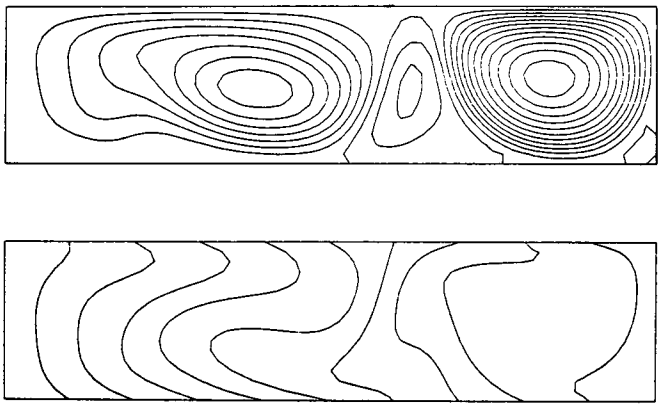

Figure 15. Typical streamlines and isotherms at $Gr = 666{,}666$ and $Pr = 0{\cdot}05$, with $L/h = 4$; finite difference results

ACKNOWLEDGEMENT

J. J. Van Schaftingen wishes to acknowledge a scholarship from the Belgian 'Fonds National de la Recherche Scientifique'.

## REFERENCES


1. S. M. Pimputkar and S. Ostrach, 'Convective effects in crystals grown from melt', *Journal of Crystal Growth*, **55**, 614–646 (1981).
2. V. I. Polezhaev, 'Hydrodynamics, heat and mass transfer during crystal growth', in *Crystals, Growth, Properties and Applications, 10*, Springer-Verlag, 1984, pp. 87–150.
3. W. E. Langlois, 'Buoyancy-driven flows in crystal-growth melts', *Ann. Rev. Fluid Mech.* **17**, 191–215 (1985).
4. J. R. Carruthers, 'Origins of convective temperature oscillations in crystal growth melts', *Journal of Crystal Growth*, **32**, 13–26 (1976).
5. D. T. J. Hurle, E. Jakeman and C. P. Johnson, 'Convective temperature oscillations in molten gallium, *J. Fluid Mech.*, **64**, 565–576 (1974).
6. J. E. Hart, 'Stability of thin non-rotating Hadley circulations', *J. Atmos. Sci.*, **29**, 687–697 (1972).
7. A. E. Gill, 'A theory of thermal oscillations in liquid metals', *J. Fluid Mech.*, **64**, 577–588 (1974).
8. J. E. Fromm, 'Numerical method for computing buoyant circulation of air in rooms', *IBM J. Res. Develop.*, **15**, 186–196 (1971).
9. M. J. Crochet, A. R. Davies and K. Walters, *Numerical simulation of non-Newtonian flow*, Elsevier, 1984.
10. M. J. Crochet, F. T. Geyling and J. J. Van Schaftingen, 'Finite element method for calculating the horizontal Bridgman growth of semi-conductor crystals', in G. F. Carey and J. T. Oden (eds), *Finite Elements in Fluids VI*, John Wiley, 321 (1985).
11. P. M. Gresho, R. L. Lee, R. Sani and T. Stullich, 'On the time-dependent solution of the incompressible Navier–Stokes equations in two and three dimensions', in *Recent Advances in Numerical Methods in Fluids*, Pineridge Press, 1980.
12. V. M. Glasov, S. N. Chizleskaya and N. N. Glagoleva, *Liquid Semiconductors*, Plenum Press, 1969.
13. A. S. Jordan, 'Estimated thermal diffusivity, Prandtl number and Grashof number of molten GaAS, in P and GaSb', *Bell Labs report* (1983).
14. A. R. Mitchell, *Computational Methods in Partial Differential Equations*, Wiley, 1969.